Int. J. Electrochem. Sci., 15 **(2020)** 1310 – 1328, doi: 10.20964/2020.02.29

International Journal of
ELECTROCHEMICAL
SCIENCE
www.electrochemsci.org

Nickel Hydroxide Nanoflakes Grown on Carbonized Melamine Foam via Chemical Bath Deposition for Supercapacitor Electrodes

Seongwoo Jeong [1†], *Jemoon Yun* [2], *Nanasaheb M. Shinde* [2], *Kyung Su Kim* [1], *Kwang Ho Kim* [1,2,*]

[1] School of Materials Science and Engineering, Pusan National University, San 30 Jangjeon-dong, Geumjeong-gu, Busan 609-735, Republic of Korea
[2] Global Frontier R&D Center for Hybrid Interface Materials, Pusan National University, San 30 Jangjeon-dong, Geumjeong-gu, Busan 609-735, Republic of Korea
[*] E-mail: kwhokim@pusan.ac.kr

Received: 1 October 2019 / *Accepted:* 27 November 2019 / *Published:* 31 December 2019

$Ni(OH)_2$ nanoflakes were deposited on a carbonized melamine foam (CMF) substrate ($Ni(OH)_2$ @CMF) via chemical bath deposition at room temperature. This was achieved by using three different $Ni(OH)_2$ precursor solution concentrations. $Ni(OH)_2$ @CMF-0.05 was obtained using a 0.05 M $Ni(OH)_2$ solution and exhibited a high specific capacitance of 1066 F g^{-1} at a specific current of 1 A g^{-1}; further, this material retained a specific capacitance of 698 F g^{-1} at a specific current of 5 A g^{-1}. At a scan rate of 5 mV s^{-1}, the specific capacitance of $Ni(OH)_2$ @CMF-0.05 was 965 F g^{-1}. This excellent electrochemical performance is ascribed to the large amount of functional groups in CMF, which allowed for its facile reaction with $Ni(OH)_2$ during the synthesis of $Ni(OH)_2$ @CMF as well as with the hydroxide ions in the electrolyte during charge/discharge cycles. The monolithic device, which was achieved owing to the three-dimensional structure of CMF, delivered a high energy density of 27.5 Wh kg^{-1} at a power density of 140 W kg^{-1} and a high power density of 7.5 kW kg^{-1} at an energy density of 6.6 Wh kg^{-1}. The device retained 100% of its energy density after 8000 charge/discharge cycles. This work suggests a potential approach to utilize melamine foam as a substrate for the low-cost growth of metal hydroxide nanostructures that can be used as electrode supercapacitors.

Keywords: $Ni(OH)_2$, N-doped carbon, melamine foam, CBD, supercapacitor

1. INTRODUCTION

As the demand for electric energy is rapidly increasing because of the growing usage of portable electronics and electric vehicles, interest in energy-storage technologies has increased. Supercapacitors, which can deliver a high power density, have attracted considerable attention. The performance of a supercapacitor is highly dependent on the electrode material. Commonly used supercapacitor electrode materials include transition-metal oxides and hydroxides such as RuO_2 [1-3], MnO_2 [4, 5], NiO [6, 7], $Ni(OH)_2$ [8], and Co_3O_4 [9-11]. Among these, $Ni(OH)_2$ is attracting interest as it is a readily available, low-cost, and ecofriendly material [12, 13]. Moreover, $Ni(OH)_2$ can exhibit a high electrode performance owing to its large specific surface area and numerous electrochemical redox reactions [14].

However, the poor electrical conductivity of $Ni(OH)_2$ limits the utilization of the surface area for the pseudocapacitive redox reaction and hinders its practical application in supercapacitors. Accordingly, combinations of $Ni(OH)_2$ with substrates having electrical conductivity and chemical stability, such as some carbon-based materials, have been investigated. [15] Numerous attempts have been made to combine $Ni(OH)_2$ with electrically conductive carbon. Wu reported that β-$Ni(OH)_2$ on graphene exhibited a high specific capacitance of 1503 F g^{-1} at a scan rate of 2 mV s^{-1} [15]. Carbon provides not only a high performance but also a low synthesis temperature. For instance, Alhebshi deposited $Ni(OH)_2$ nanoflakes on carbon fibers via chemical bath deposition (CBD) at room temperature. The resulting material exhibited a specific capacitance of 1420 F g^{-1} at a specific current of 1 A g^{-1} [14].

Nevertheless, numerous carbon sources, such as graphene, carbon nanofibers (CNFs), and carbon nanotubes, are expensive and difficult to obtain for commercial applications. In this regard, carbon foam (CF) derived from melamine foam (MF), which is readily available, is suitable [16]. MF is a three-dimensional (3D)-structured polymer resin composed of melamine ($C_3H_6N_6$), formaldehyde (CH_2O), and sodium bisulfite ($NaHSO_3$) [17]. The MF, which exhibits limited utilization as a substrate with the grown nanostructure owing to the low carbon yield, can demonstrate to be an excellent CF when subjected to simple carbonization under a N_2 atmosphere [17]. The interconnected 3D structure of carbonized MF (CMF), which has a high porosity of up to 99.6%, allows monolithic electrodes to increase the electrical conductivity to up to 6.8×10^{-2} S cm^{-1} because a binder is not needed to assemble a cell [16-20]. Additionally, the 3D structure of CMF facilitates electron transfer during charge/discharge cycles [21, 22], and its porosity endows it with an ultralight weight of 5 mg cm^{-3} [17].

N [19, 20, 23], S [24-26], and P [23, 27] are widely used in carbon-based electrode materials to reduce the intrinsic resistivity and facilitate electrolyte ion transfer. When MF is carbonized under an inert atmosphere, it transforms into a pseudocapacitive N-doped CF owing to the abundance of N in melamine [19, 20]. N, O, and several functional groups have many advantages as electrode materials or supporting substrates. Positively charged quaternary and pyridinic-N-oxide N facilitates electron transfer [28-30]. Additionally, in alkaline electrolytes, pyrrolic-type N and phenol-/carboxyl-oxygen functional groups contribute to the electrode pseudocapacitance [28-30]. The carboxyl and phenol groups in CMF, as well as the pyrrole-type N (N-5), can react with hydroxides to increase the pseudocapacitance [31]. The phenol-/carboxyl-oxygen group in CMF was reported to improve its carbon wettability and electrolyte infiltration [32]. In alkaline electrolytes, these features allow CMF to contribute to the electrode pseudocapacitance and facilitate the deposition of metal hydroxides.

Despite these significant advantages, metal oxide/hydroxides on CMF have not been reported since MnO_2@ CMF was investigated by He [16]; this is possibly due to the strong hydrophobicity of CMF [16]. The pretreatment of CMF with zinc chloride [19], CTAB [33], or acidic solutions [27, 34, 35] is known to mitigate the above-mentioned challenge. These treatments help remove impurities from the CMF surface and activate the surface for the deposition of heteroatoms or transition metals. A conventional acid treatment was also reported to introduce functional groups such as carboxyls, hydroxyls, and carbonyls that can serve as nucleation sites for the growth of $Ni(OH)_2$ [34]. In this study, we designed and fabricated $Ni(OH)_2$ nanoflakes via CBD and anchored these nanoflakes on a CMF substrate that was previously functionalized via surface modification with HCl. The $Ni(OH)_2$ nanoflakes exhibited pseudocapacitance, while the CMF substrate served as a conductive backbone that facilitated electron transfer. Moreover, an asymmetric device based on pristine CMF and $Ni(OH)_2$ @CMF exhibited an energy density of up to 27.5 Wh kg^{-1} at a power density of 140 W kg^{-1}, retaining 100% cyclic stability after 8000 cycles. The functional species and electrochemical performance of this device were investigated. This work provides insights into hydroxide-induced pseudocapacitance due to the changed composition of the functional species.

2. EXPERIMENTAL SECTION

2.1. Materials

MF (9.04 kg/m^3, Sunday), hydrochloric acid (HCl, Junsei), nickel nitrate hexahydrate ($Ni(NO_3)_2 \cdot 6H_2O$, 99%, Sigma–Aldrich), ammonium fluoride (NH_4F, 98%, Sigma–Aldrich), and Ni foam substrates (110 PPI, $320 g/m^2$, Artenano Company Limited, Hong Kong) were used as received.

2.2 CMF preparation

First, MF samples were cut to a size of 15 × 15 × 30 mm^3 and transferred to a tube vacuum furnace. After a vacuum was applied, the MF samples were heated to 1000 °C at a heating rate of 3 °C min^{-1} for 1 h under a flowing N_2 atmosphere.

2.3 Pretreatment of CMF

The obtained CMF samples were pretreated with 0.1 M HCl for 0.5 h under sonication to remove impurities and activate their surface. The samples were then rinsed with deionized water to remove any remaining HCl.

2.4 Deposition of nickel hydroxide on CMF

Three different concentrations of a $Ni(OH)_2$ precursor solution (0.025, 0.05, and 0.075 M) were synthesized by mixing $Ni(NO_3)_2 \cdot 6H_2O$ and NH_4F in deionized water. Then, the CMF samples were immersed and stirred in each solution for 12 h at room temperature. The treated CMF samples were denoted as $Ni(OH)_2$ @CMF-0.025, $Ni(OH)_2$ @CMF-0.05, and $Ni(OH)_2$ @CMF-0.075.

2.5 Assembly of asymmetric supercapacitor

An asymmetric supercapacitor was assembled with 0.7 mg of $Ni(OH)_2$ @CMF-0.05 as the positive electrode and 2.3 mg of pristine CMF as the negative electrode. A 6 M KOH solution was used as the electrolyte.

2.6 Structural characterization

The samples were characterized using X-ray diffraction (XRD, Cu K-α radiation, 40 kV, 40 mA, D8-Discover Bruker) at a scanning speed 0.2° s^{-1} over the 2θ range of 10°–80°. The surface morphology was examined using scanning electron microscopy (SEM, 5 kV, Hitachi, S-4800) and high-resolution transmission electron microscopy (TEM, JEOL, JEM–2010F). The valence of the prepared samples was determined via X-ray photoelectron spectroscopy (XPS, VG Scientifics ESCALAB250), where the C 1s peak was calibrated to 284.6 eV. Fourier transform infrared (FT-IR) spectra were recorded using a ZnSe prism in a Tensor 27 spectrometer (Bruker, Germany), where the angle of incidence was 45°, and data were recorded in the range of 4000–400 cm^{-1}. For these FT-IR analyses, 200 scans were obtained and the result was averaged with a resolution of 4 cm^{-1}.

2.7 Electrochemical characterization

The electrochemical properties were measured using a three-electrode configuration and a 6 M KOH electrolyte solution at room temperature. Pt foil and Hg/HgO were used as the counter and reference electrodes, respectively. Ni foam was used as a current collector. The samples loaded on the foam had an active mass of approximately 1 mg. The weight of the CF was not counted, because its contribution to the capacitance was marginal. The spacing between the working, counter, and reference electrodes was approximately 1 cm. Electrochemical impedance spectroscopy (EIS) (Bio-Logic VMP3) was performed in the frequency range of 500 kHz to 10 mHz with an amplitude of 14.2 mV. Cyclic voltammetry (CV) curves and galvanostatic charge/discharge (GCD) curves were measured using an electrochemical workstation (IVIUM system, nState) within potential ranges of 0–0.5 V for the half-cells and 0–1.5 V for the asymmetric device. The scan rate used to obtain the CV curves of both devices was varied from 5 to 100 mV s^{-1}. The GCD current density was varied from 0.5 to 5 Ag^{-1} for the half-cells and from 0.25 to 5 Ag^{-1} for the asymmetric device. The cyclic retention was measured at a specific current of 5 A g^{-1} for 2000 cycles for the half-cells and 8000 cycles for the asymmetric device. The specific capacitance according to the scan rate and current density was calculated using Eqs. 1–3, as described in the Electronic Supplementary Information (ESI). For the negative electrode, the mass of the CMF was included as the active mass because it contributed a specific capacitance of 245 F g^{-1} at a specific current of 0.5 A g^{-1} for the negative potential range.

3. RESULTS AND DISCUSSION

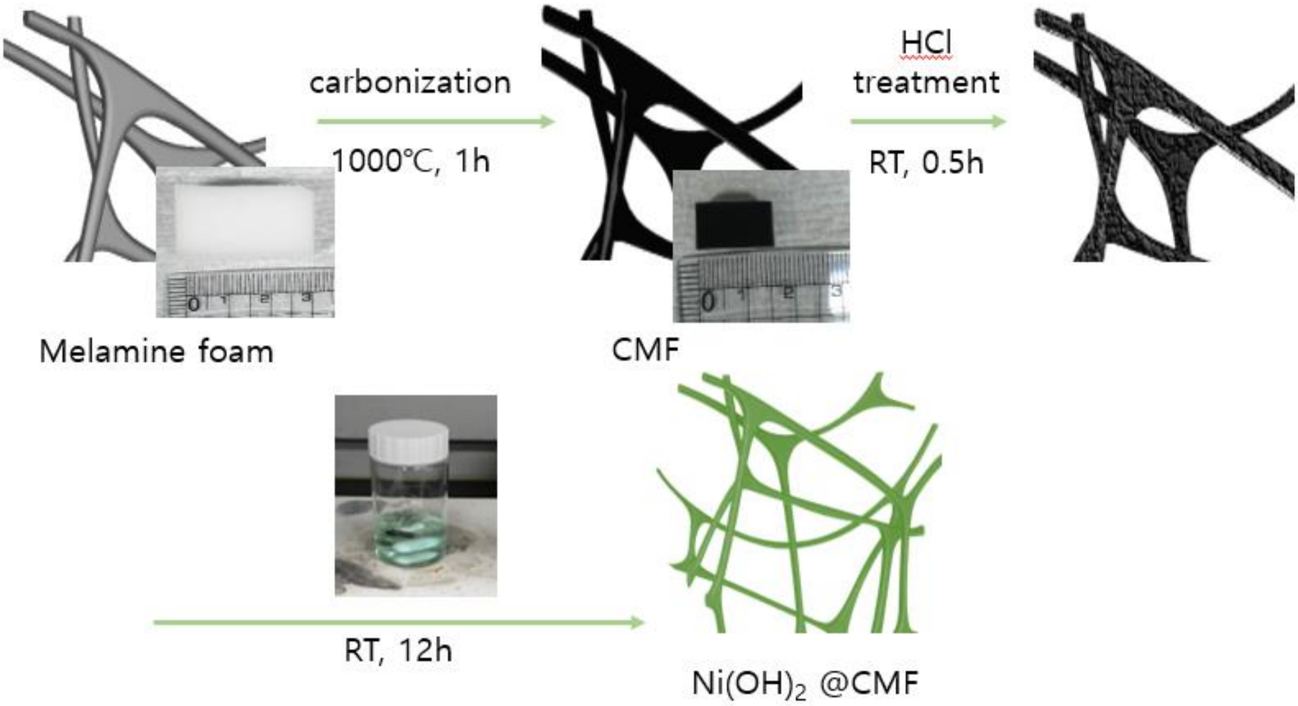

Scheme 1. Schematic illustration of the $Ni(OH)_2$ @CMF synthesis process. The first step is the carbonization of the MF. The second step is the surface modification of CMF with HCl treatment. The third step is the deposition of $Ni(OH)_2$ on the CMF substrate via CBD.

3.1 Synthesis

As the MF was carbonized at the first step, its color tuned black, and its volume decreased by 1/8 (from 6.75 to 0.843 cm^3). The density of the obtained CMF was 0.67 kg m^{-3}. The porosity of CF is 99.66% according to the equation proposed by Chen et al [17, 36]. Ni^+ and OH^- created nuclei on the activated surface during the CBD process.

3.2 Structural analysis

The XRD patterns in Fig. 2(a) indicate that the nanoparticles on the CMF had mixed $\beta-Ni(OH)_2$ and $4Ni(OH)_2$-NiOOH phases. $Ni(OH)_2$ was formed via the following mechanism [37, 38]:

$$Ni^{2+} + 2OH^- \rightarrow Ni(OH)_2. \qquad (1)$$

$Ni(OH)_2$ was then oxidized to the $\beta-NiOOH$ phase by nitrate anions via the following heterogeneous reaction [14]:

$$2Ni(OH)_2 + N_2O_6^{2-} \rightarrow 2NiOOH + 2(NO_3)^{2-} + 2H^+. \qquad (2)$$

$Ni(OH)_2$ @CMF-0.05 exhibited the sharpest and highest peaks at 19° and 33°, corresponding to the $\beta-Ni(OH)_2$ (001) and $4Ni(OH)_2NiOOH$ (101) planes, respectively [14, 39]. The peaks at 28° and 38° corresponded to the (101) and (002) planes, respectively, of $\beta-Ni(OH)_2$ [14, 39]. The peaks for $Ni(OH)_2$ @CMF-0.05 had higher intensities than those for $Ni(OH)_2$ @CMF-0.075. Furthermore,

$Ni(OH)_2$ @CMF-0.75 exhibited smaller but more numerous sharp peaks than $Ni(OH)_2$ @CMF-0.05. This peak distribution indicates that the nanostructure did not grow in a single direction but rather in many different directions, suggesting its large size.

FT-IR analyses were performed to investigate the bonding status of pristine and modified CMFs, as shown in Fig. 1(b). For all the samples, the peaks at ~3440 cm^{-1} correspond to the N-H stretching vibration [40, 41]. The intensity of this peak was lower for the $Ni(OH)_2$ @CMFs than for the CMF, indicating that the N-5 of the CMF was engaged in the synthesis reaction. For all the samples, the peaks at ~3150 cm^{-1} correspond to the O-H vibration of the water molecules [42]. For all the samples, the peaks at ~1630 cm^{-1} correspond to the stretching vibrations of C=X (X: C, N, or O), indicating the heteroatoms in the pristine and modified CMF [43]. For all the samples, the peaks at ~1460 cm^{-1} correspond to the bending vibration of C-OH [44]. With the increasing precursor solution concentration, the peak intensity increased, indicating that the material actively reacted with the hydroxide. For all the samples, the peak at ~845 cm^{-1} corresponds to the vibration of the phenol group (O-II) [45]. The higher intensity of the peak at ~845 cm^{-1} for the $Ni(OH)_2$ @CMFs compared with the CMF indicates that the amount of phenol groups (O-II) increased as CMF reacted with $Ni(OH)_2$.

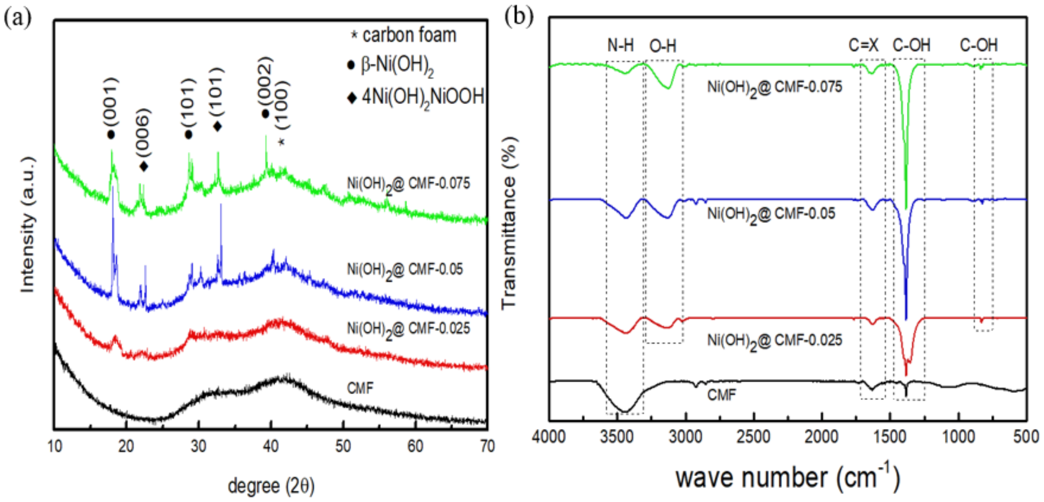

Figure 1. (a) XRD patterns and (b) FT-IR spectra of CMF and $Ni(OH)_2$ @CMFs.

The morphologies of the pristine and modified CMF samples were investigated using SEM. Fig. 2(a) shows that the pristine CMF had skeleton strands. $Ni(OH)_2$ @CMF-0.05 exhibited nanoflake structures ranging from 6 to 15 μm in size, as shown in Fig. 2(b). The elemental mapping of C, O, and Ni in Fig. 2(c), corresponding to the magnified image of Fig. 2(b), was examined via energy-dispersive X-ray spectroscopy (EDX). C, O, and Ni were evenly distributed throughout the nanostructure of $Ni(OH)_2$ @CMF-0.05. As shown in Fig. 2(d), the C was more distributed on the background of the nanostructure. In contrast, as shown in Figs. 2(d) and (e), most of the O and Ni was distributed on the nanostructure rather than on the background.

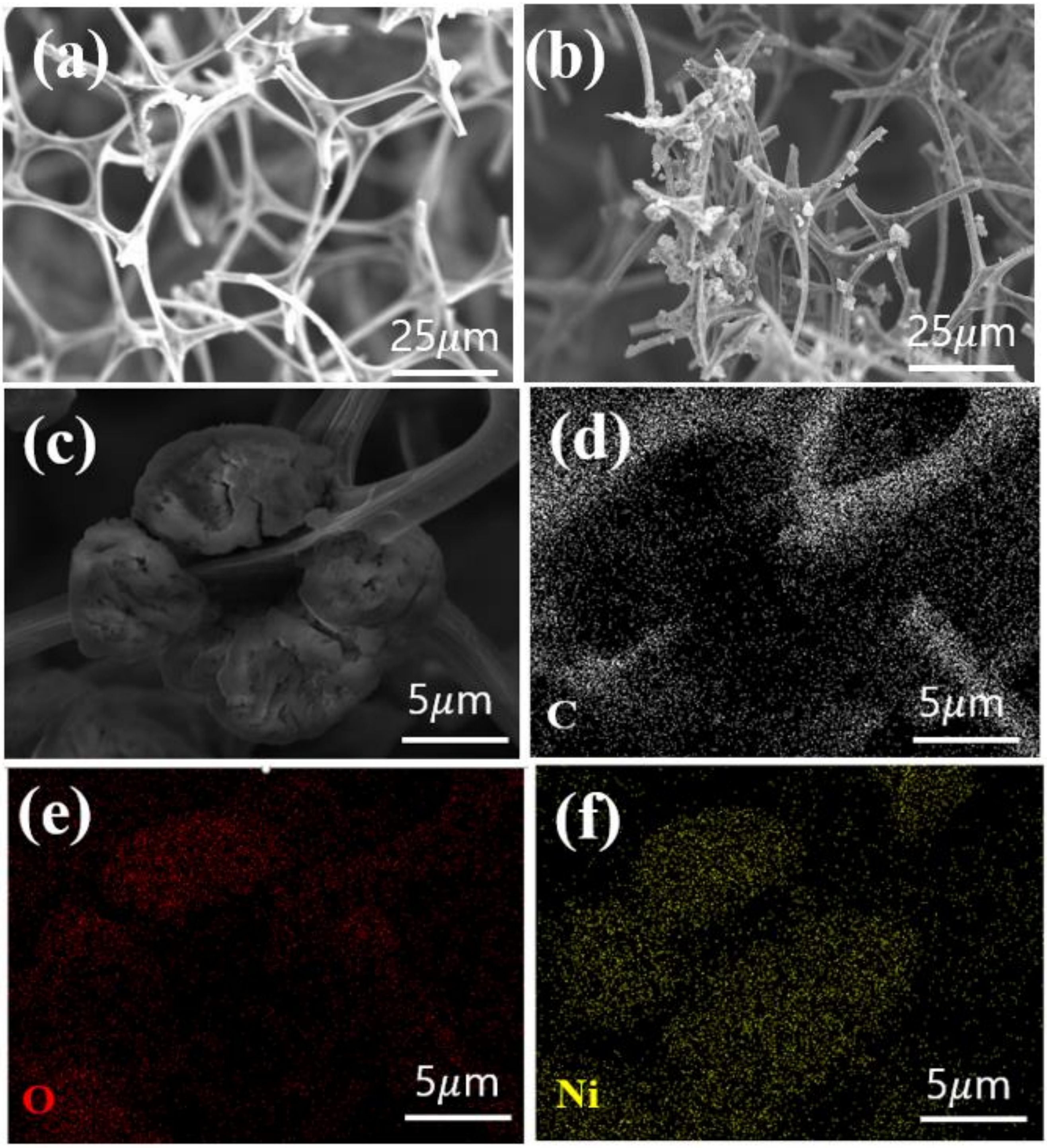

Figure 2. SEM images of (a) CMF and (b, c) $Ni(OH)_2$ @CMF-0.05. (d) C, (e) O, and (f) Ni EDX elemental mapping of $Ni(OH)_2$ @CMF-0.05.

The fine nanoflakes of $Ni(OH)_2$ @CMF-0.05 shown in Fig. 3(a) were examined using TEM. The elemental mapping of Ni and O in the image in Fig. 3(b) was investigated. As shown in Fig. 3(c), the distributions of Ni and O were in accordance with the nanostructure in Fig. 3(a) and the EDX elemental mapping results in Figs. 2(d)–(f).

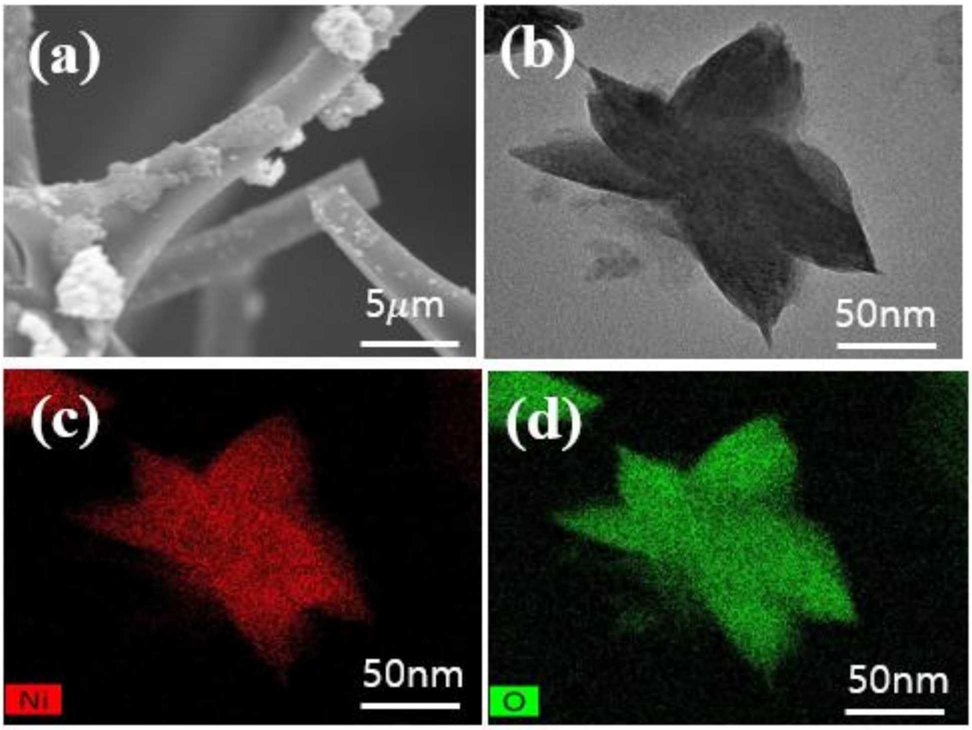

Figure 3. (a) SEM image, (b) TEM image, and (c) Ni and (d) O EDX elemental mapping of the $Ni(OH)_2$ @CMF-0.05 nanoflakes.

The elemental composition and chemical bonds of the samples were investigated using XPS, and the results are shown in Fig. 4. Peaks corresponding to C 1s (~285 eV), N 1s (~399 eV), O 1s (~532 eV), and Ni 2p (~870 eV) were observed. The peaks for C 1s, N 1s, and O 1s were each deconvoluted into four peaks. For the C1s XPS spectra, four peaks were observed, corresponding to C-C or C=C at 284.7 eV, C=N at 285.5 eV, C-O at 286.3 eV, and C=O at 287.5 eV [46]. The N 1s peaks were fitted to pyridinic-type N (N-6) at 398.5 eV, N-5 at 400.1 eV, quaternary-type N (N-Q) at 401.1 eV, and pyridinie-N-oxide (N-X) at 403 eV [46-48]. The positive charges of N-X and N-Q are reported to contribute to the electron transfer in bulk carbon and have a dominant effect on the capacitive behavior [49]. In alkaline solutions, N-5 is the only N species that contributes to the pseudocapacitance [19]. The O 1s XPS spectra were fitted to quinone-type O (O-I) at 531 eV, phenol-type O (O-II) at 532.3 eV, ether-type O (O-III) at 533.5 eV, and carboxyl-type O (O-IV) at 534.5 eV [19]. The carboxyl type (O-IV) peak at 534.5 eV indicates that the hydroxide was bound to C, forming a carboxyl group. The carboxyl (O-IV) and phenol groups (O-II) contribute to the pseudocapacitance in alkaline electrolytes through faradaic redox reactions [19]. Two peaks for Ni 2p belonging to Ni $2p_{3/2}$ at 855.6 eV and Ni $2p_{1/2}$ at 873.1 eV were observed. The C=N peaks at 285.5 eV confirmed the doping of N in the CMF [19]. The Ni 2p peak indicated the presence of Ni^{2+} [50]. The atomic contents of the active species, including N-5, O-II, O-IV, and Ni, are compared in Table 1. As N-5 reacted with the hydroxide during the synthesis reaction, the atomic contents of N-5 decreased with the increasing precursor solution concentration. The amounts of N-Q and N-X decreased as the precursor solution concentration increased to 0.075 M. The largest amounts of O-II and O-IV were detected in $Ni(OH)_2$ @CMF-0.05 and $Ni(OH)_2$ @CMF-0.075, respectively. The largest amount of Ni was detected in $Ni(OH)_2$ @CMF-0.075, but it was <1% larger than that for Ni(OH)$_2$ @CMF-0.075. This result is in accordance with the FT-IR results and Ni(OH)$_2$ precursor solution concentration.

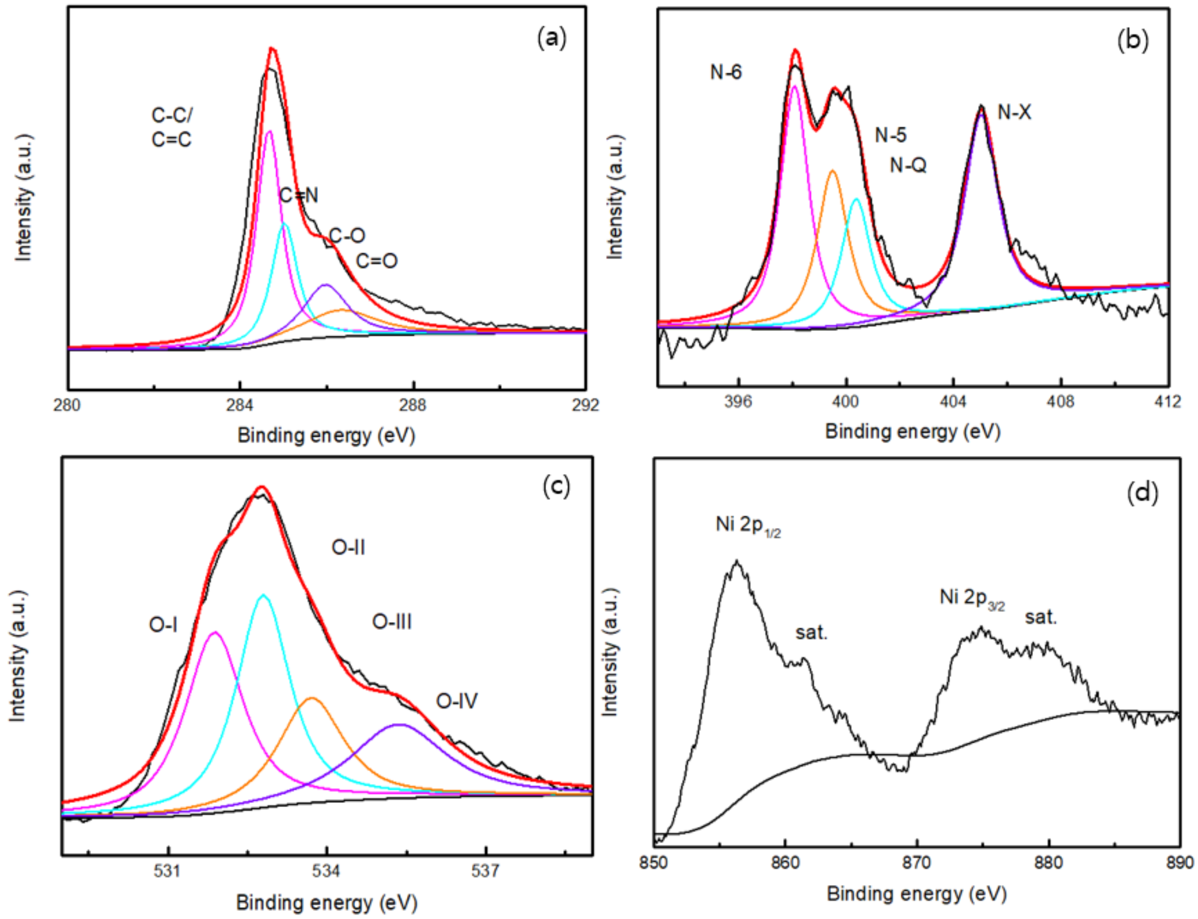

Figure 4. XPS fitted spectra of (a) C 1s, (b) N 1s, and (c) O 1s and XPS survey results of (d) Ni 2p for Ni(OH)$_2$ @CMF-0.05.

Table 1. Atomic contents of N, O, and Ni in the CMF and Ni(OH)$_2$ @CMFs, determined via XPS.

		N-6	N-5	N-Q	N-X	O-I	O-II	O-III	O-IV	Ni
CMF		0.67	0.51	1.0	0.34	0.02	5.27	1.85	0.81	0
Ni(OH)$_2$ @CMF-	0.025	1.37	1.80	0.58	1.29	3.41	5.34	9.38	0.80	4.37
	0.05	2.44	1.70	1.65	1.79	3.16	6.93	4.92	7.62	27.84
	0.075	2.07	1.11	1.33	1.26	3.38	14.92	8.45	1.57	28.73

3.3 Electrochemical analysis

The electrochemical properties of the pristine and modified CMFs were investigated using CV. As shown in Figs. 3(a) and (b), in a 6 M KOH electrolyte solution, the Ni(OH)$_2$ @CMFs exhibited pseudocapacitance. In alkaline electrolytes, the N-5 and the carboxyl and phenol groups in CMF contribute to the pseudocapacitance, as indicated by a previous study [31, 46]. The redox reaction of the $Ni(OH)_2$ @CMFs is attributed to O-II and $Ni(OH)_2$, as follows:

$$Ni(OH)_2 + OH^- \leftrightarrow NiOOH + H_2O + e^-. \qquad (3)$$

In Fig. 5(a), the redox peaks of the $Ni(OH)_2$ @CMF samples are in different locations owing to the different phases present, in accordance with the XRD results in Fig. 1(a). The CV curves of $Ni(OH)_2$ @CMF-0.05 retained their shape even at a high scan rate of 100 mV s^{-1}, as shown in Fig. 5(b), indicating the proper hybridization of $Ni(OH)_2$ with CMF [51]. This proper hybridization resulted in an efficient ion diffusion at the electrode–electrolyte interface. Therefore, both the exterior and interior pore surfaces of the hybrid electrode material were effectively utilized for intercalation. The specific capacitance was measured as a function of the scan rate. $Ni(OH)_2$ @CMF-0.05 exhibited a specific capacitance of 935 F g^{-1} at a scan rate of 5 mV s^{-1}. At the same scan rate, CMF, $Ni(OH)_2$ @CMF-0.025, and $Ni(OH)_2$ @CMF-0.075 exhibited specific capacitances of 84.6, 105.4, and 482.9 F g^{-1}, respectively. These results agree with the CV curves. The specific capacitance of $Ni(OH)_2$ @CMF-0.05 was 935.5 F g^{-1}, as calculated using Eq. (1) in the ESI, at a scan rate of 5 mV s^{-1}. Using the same scan rate, the specific capacitances of CMF, $Ni(OH)_2$ @CMF-0.025, and $Ni(OH)_2$ @CMF-0.075 were 84.6, 105.4, and 482.9 F g^{-1}, respectively. These results are consistent with the CV results.

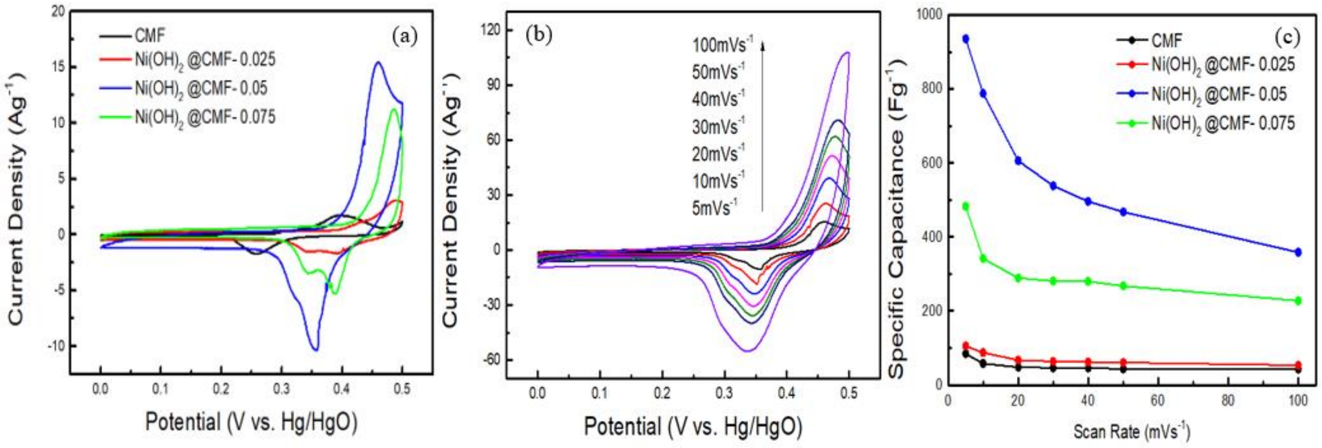

Figure 5. CV curves of (a) CMF and $Ni(OH)_2$ @CMFs at 50 mV s^{-1}; and (b) $Ni(OH)_2$ @CMF-0.05 at various scan rates (5–100 mVs^{-1}). (c) Specific capacitance as a function of scan rate of CMF and $Ni(OH)_2$ @CMFs.

Fig. 6(a) shows the GCD curves of the $Ni(OH)_2$ @CMFs at a specific current of 0.5 A g^{-1}. At a specific current of 1 A g^{-1}, the specific capacitance of $Ni(OH)_2$ @CMF-0.05 was 1066 F g^{-1}, and those of CMF, $Ni(OH)_2$ @CMF 0.025, and $Ni(OH)_2$ @CMF 0.025 were 90.6, 172.2, and 615.8 F g^{-1}, respectively. The higher electrochemical performance of $Ni(OH)_2$ @CMF-0.05 and $Ni(OH)_2$ @CMF-0.075 is attributed to their abundant active species, such as N-5, O-II, O-IV, and Ni. Although $Ni(OH)_2$ @CMF-0.75 had larger amounts of O-II and Ni than $Ni(OH)_2$ @CMF-0.05, it exhibited a lower specific capacitance than $Ni(OH)_2$ @CMF-0.05 owing to its lower amount of N-5, which can react with two hydroxides in the exchange of two electrons [19]. Fig. 6(d) shows the EIS results. Here, the x-intercepts in the high-frequency area indicate the serial resistance, which was the sum of the intrinsic resistance, electrolyte resistance, and contact resistance between the electroactive material and the current collector. The slope of the line in the low-frequency area indicates the diffusion resistance related to the double-layer capacitance. According to the Nyquist plots of the $Ni(OH)_2$ @CMFs, increasing the $Ni(OH)_2$ precursor solution concentration to 0.05 M reduced the serial resistance and increased the diffusion resistance. The charge-transfer resistance of $Ni(OH)_2$ @CMF-0.75 is attributed to decreases in N-Q and N-X, which contribute to electron transfer in bulk carbon [49].

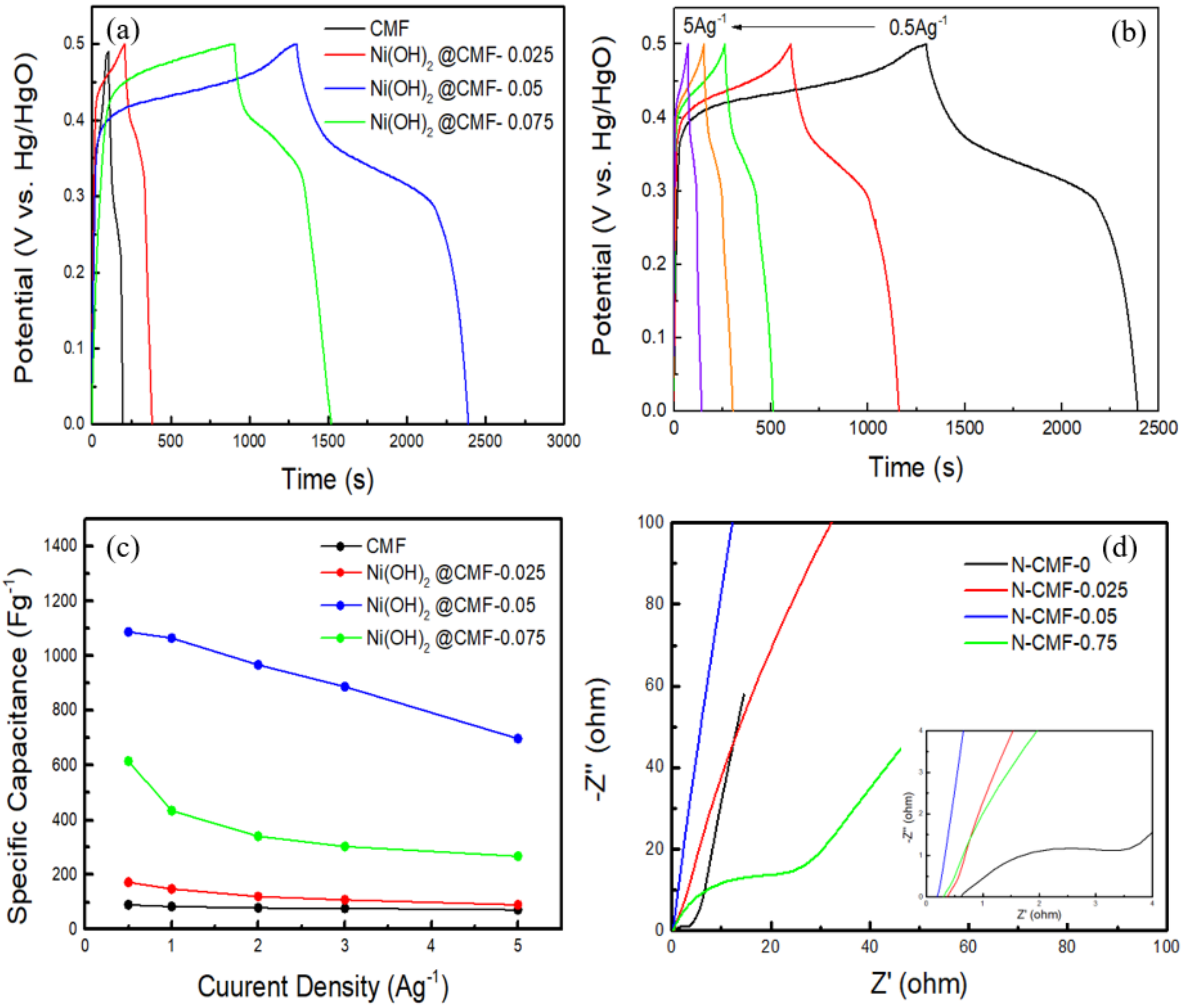

Figure 6. (a) GCD curves of CMF and $Ni(OH)_2$ @CMFs at a specific current of 0.5 A g^{-1}. (b) GCD curves of $Ni(OH)_2$ @CMF-0.05 at various specific currents (0.5–5 Ag^{-1}). (c) Specific capacitance with respect to the specific current (0.5–5 Ag^{-1}). (d) Nyquist plots of CMF and $Ni(OH)_2$ @CMFs.

The electrochemical performance of the asymmetric CMF/$Ni(OH)_2$ @CMF-0.05 device is shown in Fig. 7. The CV curves of the asymmetric device in Fig. 7(b) agree with the CV curves of CMF and $Ni(OH)_2$ @CMF-0.05 in Fig. 7(a). The specific capacitance of the device was 88 F g^{-1}, which is significantly lower than that of the $Ni(OH)_2$ @CMF-0.05 half-cell owing to the relatively low specific capacitance of the negative electrode (Fig. S6). As shown in Fig. 7(c), the power density of the device was 3 and 0.14 kW kg^{-1} at an energy density of 12.1 and 27.5 Wh kg^{-1}, respectively, as calculated using

Eqs. (4) and (5) in the ESI. These values are higher than those of a CNF-based composite [14] and comparable to the performance of a Ni-foam-based composite fabricated through high-temperature hydrothermal synthesis [52]. The device retained 100% of its specific capacitance after 8000 charge/discharge cycles. In comparison, $Ni(OH)_2$ @CMF-0.05 enveloped by Ni foam retained 47% of its specific capacitance after 2000 cycles (Fig. S5). As shown in Fig. 7(f), a light-emitting diode (LED) was powered at maximum brightness using the CMF/$Ni(OH)_2$ @CMF-0.05 devices.

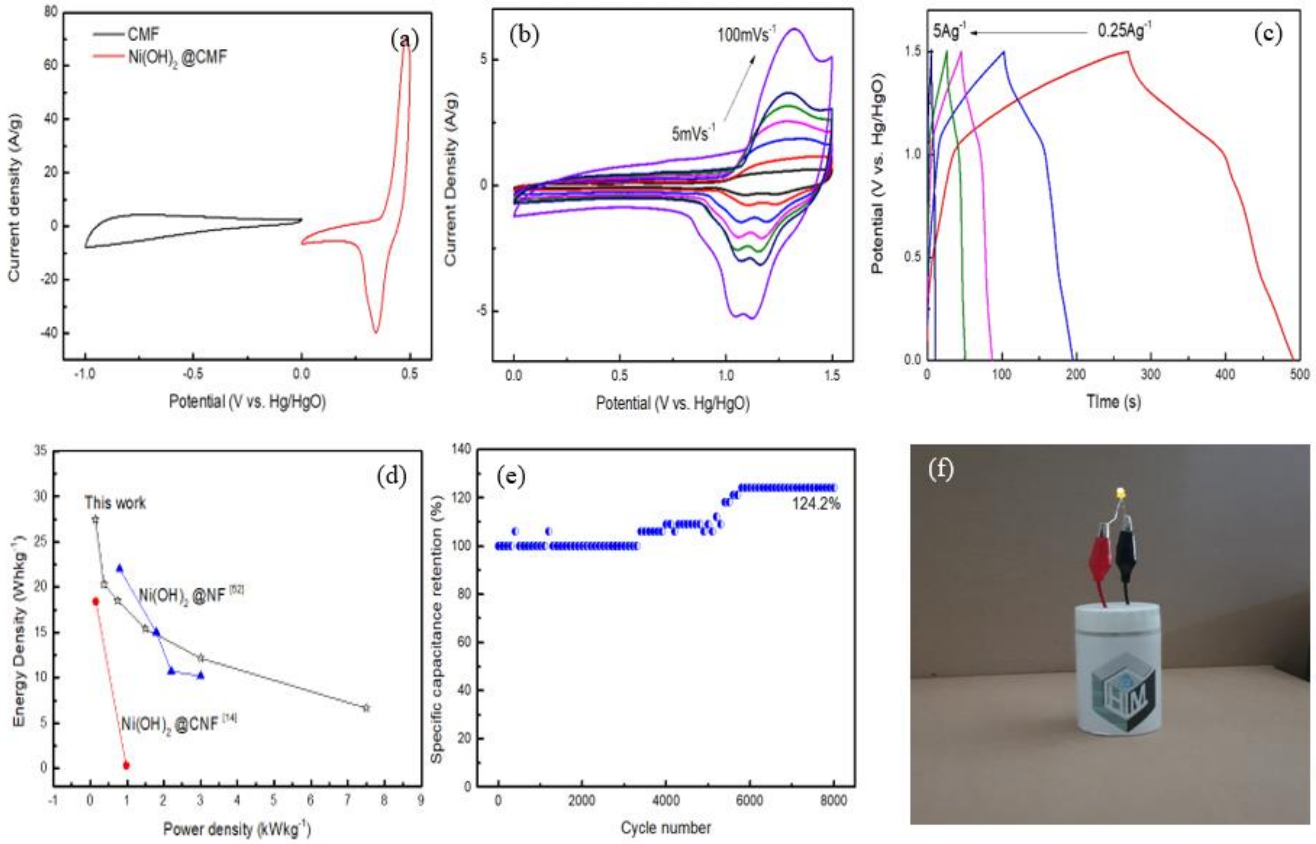

Figure 7. (a) CV curves of CMF and $Ni(OH)_2$ @CMF-0.05 at 50 mVs^{-1}. Electrochemical performance of the asymmetric CMF/$Ni(OH)_2$ @CMF-0.05 device, including (b) CV curves obtained at various scan rates, (c) GCD curves obtained at various current densities, (d) the Ragone plot, (e) the capacitance retention with respect to the cycle number, and (f) illumination of an LED using the CMF/$Ni(OH)_2$ @CMF-0.05 asymmetric device.

4. CONCLUSIONS

In this study, $Ni(OH)_2$ nanoflakes were deposited on CMF via CBD at room temperature. $Ni(OH)_2$ @CMF-0.05 exhibited a specific capacitance of 1066 F g^{-1} at a specific current of 1 A g^{-1}. This high performance was attributed to its high electrical conductivity as a result of non-directional crystal growth and a large number of active species. The asymmetric CMF/$Ni(OH)_2$ @CMF-0.05 device exhibited an energy density of 27.5 Wh kg^{-1} at a power density of 140 W kg^{-1} without any energy-density loss up to 8000 charge/discharge cycles. This performance was higher than that of CNF-based $Ni(OH)_2$ and comparable to that of a Ni-foam-based device. Given the availability and low cost of $Ni(OH)_2$ and MF, as well as the excellent performance of the assembled device, $Ni(OH)_2$ is a promising commercial pseudocapacitor.

ACKNOWLEDGEMENTS
We gratefully acknowledge the support for this work from the Global Frontier Program through the Global Frontier Hybrid Interface Materials (GFHIM) of the National Research Foundation of Korea (NRF) funded by the Ministry of Science, ICT & Future Planning (2013M3A6B1078874). The authors are very grateful to the members of the National Core Research Centre (NCRC) for their excellent experimental assistance.

SUPPORTING INFORMATION

Electrochemical characterization

The specific capacitance ($C_{S,CV}$, Fg^{-1}) as a function of the CV scan rate was calculated as follows:

$$C_{S,CV} = \int i(V)dV/mv\Delta V \qquad (1)$$

where $i(V)$ represents the voltammetric current (A), m represents the mass of the active materials (g) loaded on the current collectors, v represents the potential scan rate (Vs^{-1}), and ΔV represents the potential window of 1 V. The specific capacitance ($C_{S,GCD}$, F g^{-1}) obtained using the GCD curves was calculated as follows:

$$C_{S,GCD} = I\Delta t/m\Delta V \qquad (2)$$

where $I, \Delta t, \Delta V,$ and m represent the applied current (A), discharge time (s), voltage change (V), and mass of the active material (g), respectively. The mass of the CF was disregarded because its contribution to the capacitance at a positive potential is negligible. The specific capacitance (C_S, Fg^{-1}) of the asymmetric device was calculated as follows:

$$C_S = 2I\Delta t/m\Delta V \qquad (3)$$

The energy density (E, Wh kg^{-1}) and power density (P, W kg^{-1}) of the device were calculated as follows:

$$E = C_S\Delta V^2/(2 * 3.6) \qquad (4)$$

$$P = E * 3600/\Delta t \qquad (5)$$

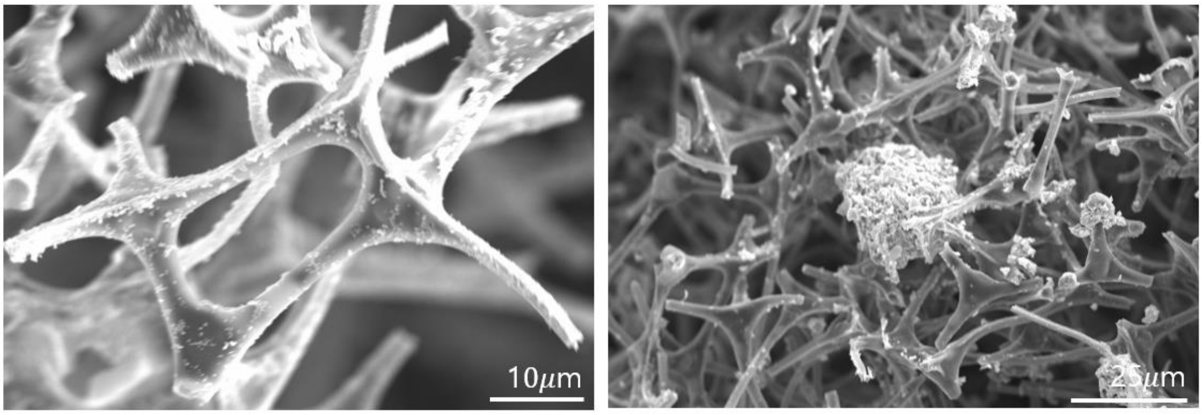

Fig. S1. SEM images of (a) $Ni(OH)_2$ @CMF-0.025; (b) $Ni(OH)_2$ @CMF-0.075.

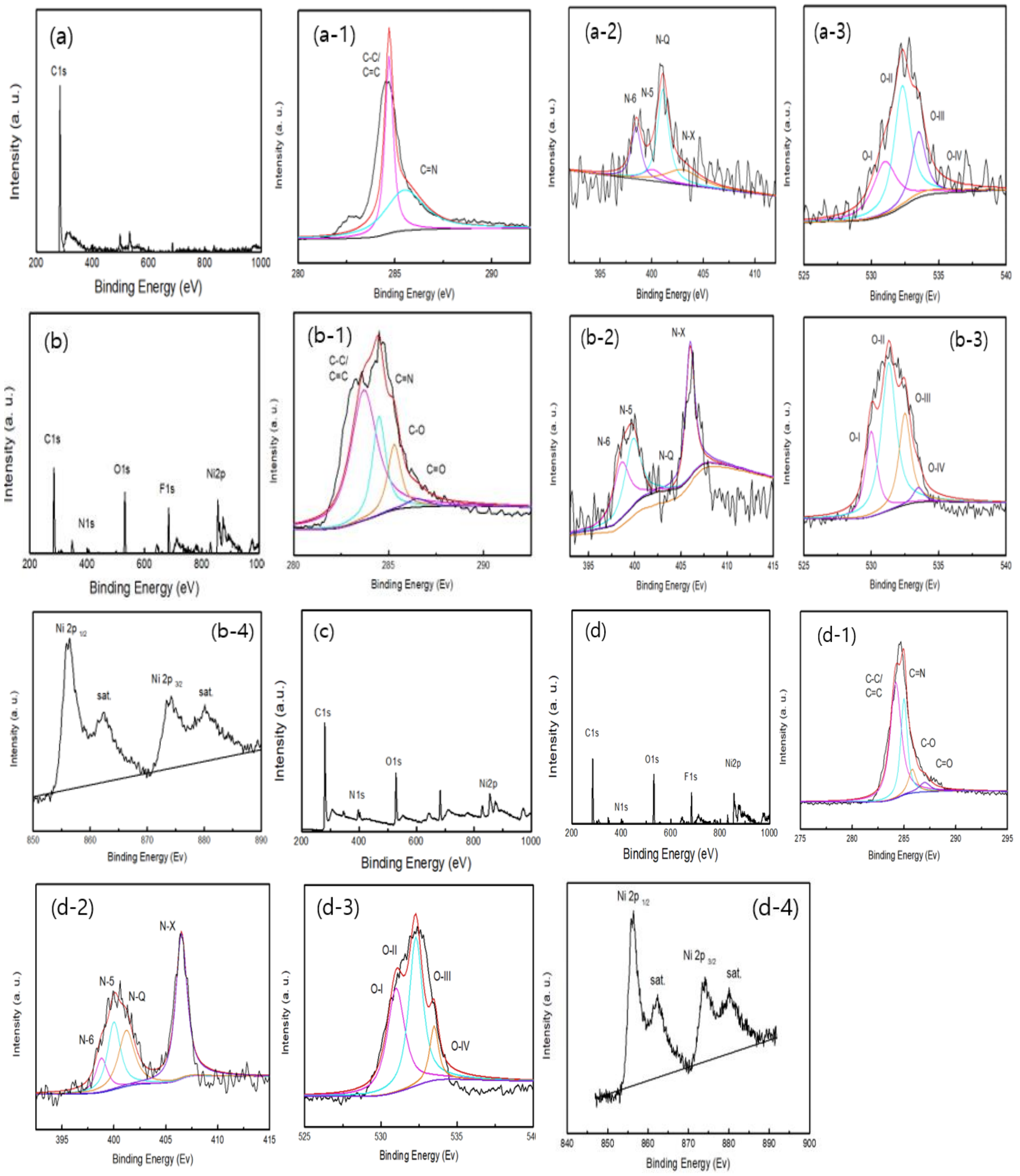

Fig. S2 XPS survey results and fitted spectra for (a–a3) CMF; (b–b4) $Ni(OH)_2$ @CMF-0.025; (c) $Ni(OH)_2$ @CMF-0.05; (d–d4) $Ni(OH)_2$ @CMF-0.075.

Table S1 Atomic contents of C 1s, N 1s, O1s, and Ni 2p in the CMF and $Ni(OH)_2$ @CMFs.

	C-C /C=C	C=N	C-O	C=O	C 1s
	N-6	N-5	N-Q	N-X	N 1s

	O-I	O-II	O-III	O-IV	O 1s	Ni 2p
CMF	76.18	9.95	2.31	1.08	89.53	
	0.67	0.51	1.00	0.34	2.52	
	1.74	4.21	1.54	0.46	7.95	0
NI(OH)$_2$ @CMF-0.025	23.58	5.33	26.01	16.75	71.66	
	1.37	1.80	0.58	1.29	5.03	
	3.41	5.34	9.38	0.80	18.94	4.37
NI(OH)$_2$ @CMF-0.05	22.58	5.67	8.40	7.84	41.97	
	2.44	1.70	1.65	1.79	7.58	
	3.16	6.93	4.92	7.62	22.62	27.84
NI(OH)$_2$ @CMF-0.075	22.23	8.45	1.92	4.53	37.14	
	2.07	1.11	1.35	1.26	5.8	
	3.38	14.92	8.45	1.57	28.32	28.13

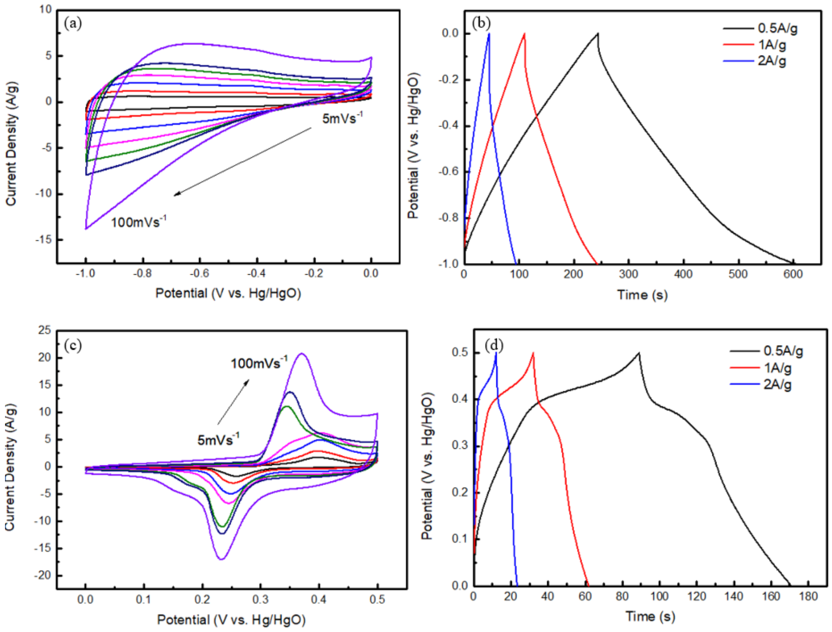

Fig. S3. (a) CV curves obtained at various scan rates (5–100 mVs^{-1}) and (b) GCD curves obtained at various specific currents (0.5–2 Ag^{-1}) for CMF at a negative potential (–1 to 0 V); (c) CV curves obtained at various scan rates (5–100 mVs^{-1}) and (d) GCD curves obtained at various specific currents (0.5–2 Ag^{-1}) for CMF at a positive potential (0–1 V).

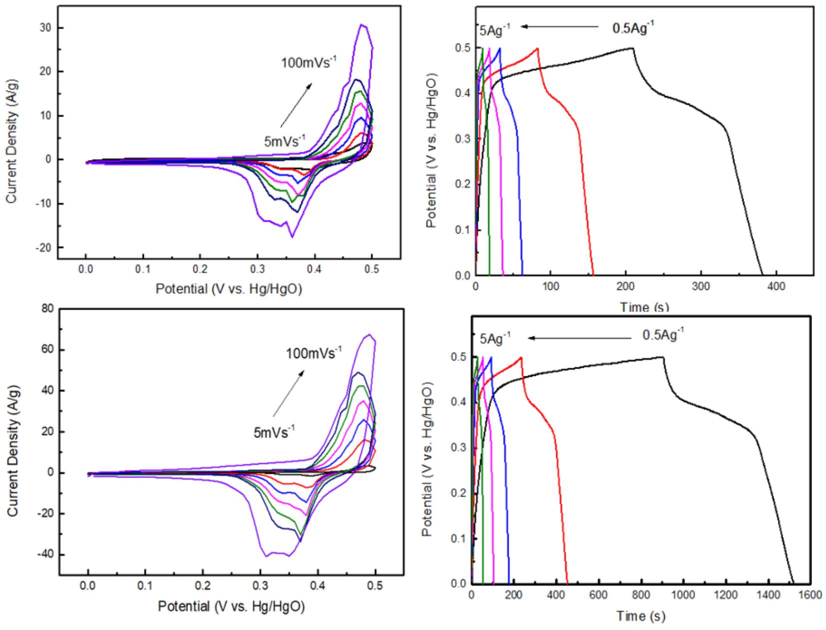

Fig. S4. (a) CV curves obtained at various scan rates (5–100 mVs^{-1}) and (b) GCD curves obtained at various specific currents (0.5–2 Ag^{-1}) for $Ni(OH)_2$ @CMF-0.025; (c) CV curves obtained at various scan rates (5–100 mVs^{-1}) and (d) GCD curves obtained at various specific currents (0.5–2 Ag^{-1}) for $Ni(OH)_2$ @CMF-0.075.

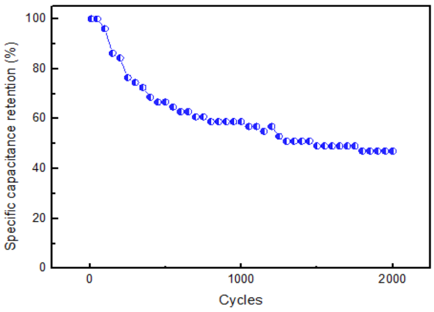

Fig. S5. Cyclic specific capacitance retention of $Ni(OH)_2$ @CMF-0.05.

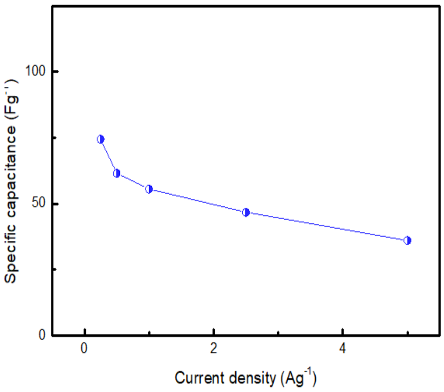

Fig. S6. Cyclic specific capacitance retention of the asymmetric CMF/$Ni(OH)_2$ @CMF-0.05 device.

Table S2. Comparison of the specific capacitance, energy density, power density, and capacitance retention with those of similar materials.

Materials	Synthesis Method / Temp. (℃)	Specific Capacitance (Fg^{-1})	Energy density ($Whkg^{-1}$) / Power density ($kWkg^{-1}$)	Capacitance retention (%) / cycle	ref.
this work	CBD / RT	1066 / 1Ag^{-1}	27.5 / 0.14 12.1 / 3	124 / 8000	
$Ni(OH)_2$ @CNF	CBD / RT	1416 / 1 Ag^{-1}	18.4 / 0.15 0.3 / 0.98	66 / 10000	14
$Ni(OH)_2$ @NF	hydrothermal/ 120	1837 / 20 Ag^{-1}	22 / 0.8 10 / 18.9	85.7 / 4000	52
$Ni(OH)_2$ @NF	CBD / RT	2384.3 / 1 Ag^{-1}	-	75 / 3000	16
$Ni(OH)_2$ @G	reflux / 95	1503 / 2mVs^{-1}	-	96.5 / 6000	15

References

1. R.-R. Bi, X.-L. Wu, F.-F. Cao, L.-Y. Jiang, Y.-G. Guo, L.-J. Wan, *J. Phys. Chem.* C, 114 (2010) 2448-2451.
2. C.-C. Hu, K.-H. Chang, M.-C. Lin, Y.-T. Wu, *Nano lett*., 6 (2006) 2690-2695.
3. T. Liu, W. Pell, B. Conway, *Electrochim. Acta*, 42 (1997) 3541-3552.

4. S. Chen, J. Zhu, X. Wu, Q. Han, X. Wang, *ACS nano*, 4 (2010) 2822-2830.
5. L. Demarconnay, E. Raymundo-Pinero, F. Béguin, *J. Power Sources*, 196 (2011) 580-586.
6. C. Yuan, X. Zhang, L. Su, B. Gao, L. Shen, *J.Mater. Chem*., 19 (2009) 5772-5777.
7. X. Zhang, W. Shi, J. Zhu, W. Zhao, J. Ma, S. Mhaisalkar, T.L. Maria, Y. Yang, H. Zhang, H.H. Hng, *Nano Res*., 3 (2010) 643-652.
8. Y. Yuan, X. Xia, J. Wu, J. Yang, Y. Chen, S. Guo, *Electrochim. Acta*, 56 (2011) 2627-2632.
9. S.K. Meher, G.R. Rao, *J. Phys. Chem*. C, 115 (2011) 15646-15654.
10. X.-h. Xia, J.-p. Tu, Y.-j. Mai, X.-l. Wang, C.-d. Gu, X.-b. Zhao, *J. Mater. Chem.,* 21 (2011) 9319-9325.
11. C. Yuan, L. Yang, L. Hou, J. Li, Y. Sun, X. Zhang, L. Shen, X. Lu, S. Xiong, X.W. Lou*, Adv. Funct. Mater*., 22 (2012) 2560-2566.
12. F.S. Cai, G.Y. Zhang, J. Chen, X.L. Gou, H.K. Liu, S.X. Dou, *Angew. Chem. Int*. Ed., 43 (2004) 4212-4216.
13. H. Wang, Y. Liang, T. Mirfakhrai, Z. Chen, H.S. Casalongue, H. Dai, *Nano Res*., 4 (2011) 729-736.
14. N.A. Alhebshi, R. Rakhi, H.N. Alshareef, *J. Mater. Chem*. A, 1 (2013) 14897-14903.
15. Z. Wu, X.-L. Huang, Z.-L. Wang, J.-J. Xu, H.-G. Wang, X.-B. Zhang, Sci. Rep., 4 (2014) 3669.
16. S. He, W. Chen, *J. Power Sources*, 262 (2014) 391-400.
17. S. Chen, G. He, H. Hu, S. Jin, Y. Zhou, Y. He, S. He, F. Zhao, H. Hou, *Energy & Environmental Science*, 6 (2013) 2435-2439.
18. P. Zhang, R. Wang, M. He, J. Lang, S. Xu, X. Yan, *Adv. Funct. Mater*. 26 (2016) 1354-1364.
19. R. Zhang, X. Jing, Y. Chu, L. Wang, W. Kang, D. Wei, H. Li, S. Xiong, *J. Mater. Chem*. A, 6 (2018) 17730-17739.
20. J. Wang, L. Shen, P. Nie, X. Yun, Y. Xu, H. Dou, X. Zhang, *J. Mater. Chem*. A, 3 (2015) 2853-2860.
21. X. Lang*, Nat. Nanotechnol*., 6 (2011) 232.
22. P. Yang, X. Xiao, Y. Li, Y. Ding, P. Qiang, X. Tan, W. Mai, Z. Lin, W. Wu, T. Li, *ACS nano*, 7 (2013) 2617-2626.
23. X. Yan, Y. Liu, X. Fan, X. Jia, Y. Yu, X. Yang, *J. Power Sources*, 248 (2014) 745-751.
24. M. Seredych, T.J. Bandosz, *J. Mater. Chem*. A, 1 (2013) 11717-11727.
25. W. Si, J. Zhou, S. Zhang, S. Li, W. Xing, S. Zhuo, *Electrochim. Acta*, 107 (2013) 397-405.
26. J. Yang, X. Zhou, D. Wu, X. Zhao, Z. Zhou, *Adv. Mater*., 29 (2017) 1604108.
27. J. Patiño, N. López-Salas, M.C. Gutiérrez, D. Carriazo, M.L. Ferrer, F. del Monte, *J. Mater. Chem*. A, 4 (2016) 1251-1263.
28. G. Sun, L. Ma, J. Ran, B. Li, X. Shen, H. Tong, *Electrochim. Acta,* 194 (2016) 168-178.
29. D. Hulicova-Jurcakova, M. Seredych, G.Q. Lu, T.J. Bandosz, *Adv. Funct. Mater*., 19 (2009) 438-447.
30. S. Wang, J. Zhang, P. Shang, Y. Li, Z. Chen, Q. Xu, *Chem. Comm.,* 50 (2014) 12091-12094.
31. Y.J. Oh, J.J. Yoo, Y.I. Kim, J.K. Yoon, H.N. Yoon, J.-H. Kim, S.B. Park, *Electrochim. Acta*, 116 (2014) 118-128.
32. Z.-H. Huang, T.-Y. Liu, Y. Song, Y. Li, X.-X. Liu, *Nanoscale,* 9 (2017) 13119-13127.
33. X. Zhao, W. Cai, Y. Yang, X. Song, Z. Neale, H.-E. Wang, J. Sui, G. Cao, *Nano Energy*, 47 (2018) 224-234.
34. J. Zhao, J. Chen, S. Xu, M. Shao, Q. Zhang, F. Wei, J. Ma, M. Wei, D.G. Evans, X. Duan, *Adv. Funct. Mater*., 24 (2014) 2938-2946.
35. D. Hulicova-Jurcakova, M. Seredych, G.Q. Lu, N. Kodiweera, P.E. Stallworth, S. Greenbaum, T.J. Bandosz, *Carbon*, 47 (2009) 1576-1584.
36. S. Chen, H. Hou, F. Harnisch, S.A. Patil, A.A. Carmona-Martinez, S. Agarwal, Y. Zhang, S. Sinha-Ray, A.L. Yarin, A. Greiner, *Energy Environ. Sci*., 4 (2011) 1417-1421.
37. P. Bukovec, N. Bukovec, B. Orel, K. Wissiak, *J. Therm. Anal*., 40 (1993) 1193-1196.
38. S.-Y. Han, D.-H. Lee, Y.-J. Chang, S.-O. Ryu, T.-J. Lee, C.-H. Chang, *J. Electrochem. Soc*., 153

(2006) C382-C386.
39. X. Xiong, D. Ding, D. Chen, G. Waller, Y. Bu, Z. Wang, M. Liu, *Nano Energy*, 11 (2015) 154-161.
40. H. Huang, X. Wei, S. Gao, *Electrochim. Acta*, 220 (2016) 427-435.
41. Y. Cai, Y. Luo, H. Dong, X. Zhao, Y. Xiao, Y. Liang, H. Hu, Y. Liu, M. Zheng, *J. Power Sources*, 353 (2017) 260-269.
42. G. Su, T. Zhou, Y. Zhang, X. Liu, A. Zhang, *Soft matter*, 12 (2016) 1145-1157.
43. C. Wang, Y. Zhou, L. Sun, P. Wan, X. Zhang, J. Qiu, *J. Power Sources*, 239 (2013) 81-88.
44. Y. Zhang, S. Xiang, G. Wang, H. Jiang, C. Xiong, *Catal. Sci. Technol*., 4 (2014) 1055-1063.
45. P. Askari, P. Zahedi, I. Rezaeian, *J. Appl. Polym. Sci*., 133 (2016).
46. Z. Zhang, Y. Zhang, X. Mu, J. Du, H. Wang, B. Huang, J. Zhou, X. Pan, E. Xie, *Electrochim. Acta*, 242 (2017) 100-106.
47. H. Li, W. Kang, L. Wang, Q. Yue, S. Xu, H. Wang, J. Liu, *Carbon*, 54 (2013) 249-257.
48. L. Wan, C. Du, S. Yang, *Electrochim. Acta*, 251 (2017) 12-24.
49. M. Seredych, D. Hulicova-Jurcakova, G.Q. Lu, T.J. Bandosz, *Carbon*, 46 (2008) 1475-1488.
50. Y. Wei, L. Yan, C. Wang, X. Xu, F. Wu, G. Chen, *J. Phys. Chem*. B, 108 (2004) 18547-18551.
51. D.P. Dubal, R. Holze, P. Gomez-Romero*, Sci. Rep.,* 4 (2014) 7349.
52. W. Sun, X. Rui, M. Ulaganathan, S. Madhavi, Q. Yan, *J. Power Sources*, 295 (2015) 323-328